Supplementary Information:

Study on mechanisms of two-step hydrogen sorption in MgH_2-TiCrMnFeZr high-entropy alloy composite

Yinghui Li,[abc] Yingyan Zhao,[a] Shusheng Cao,[ab] Zi Li,[ab] Yueqing Shen,[c] Yasemen Kuddusi,[c] Chong Lu,[d] Xi Lin,[a] Andreas Züttel,[c] Chongnan Ye*[c], Jianxin Zou*[ab]

[a.] Shanghai Key Laboratory of Hydrogen Science & Center of Hydrogen Science, Shanghai Jiao Tong University, Shanghai, 200240, PR China

[b.] National Engineering Research Center of Light Alloys Net Forming & State Key Laboratory of Metal Matrix Composites, Shanghai Jiao Tong University, Shanghai, 200240, PR China

[c.] Institute of Chemical Sciences and Engineering, Basic Science Faculty, École Polytechnique Fédérale de Lausanne (EPFL) Valais/Wallis, Energypolis, Sion, 1951, Switzerland

[d.] Instrumental Analysis Center of SJTU, Shanghai Jiao Tong University, Shanghai, 200240, PR China

*E-mail for C. Y.: chongnan.ye@epfl.ch;

*E-mail for J. Z.: zoujx@sjtu.edu.cn

Table S1 The inductively coupled plasma (ICP) results of TiCrMnFeZr HEA and MgH_2-40 wt% TiCrMnFeZr composite (wt%).

Elements	TiCrMnFeZr	MgH_2-40 wt% TiCrMnFeZr
Mg	-	54.27
Ti	27.28	10.96
Cr	25.55	10.26
Mn	33.81	13.56
Fe	3.57	1.43
Zr	10.51	4.28

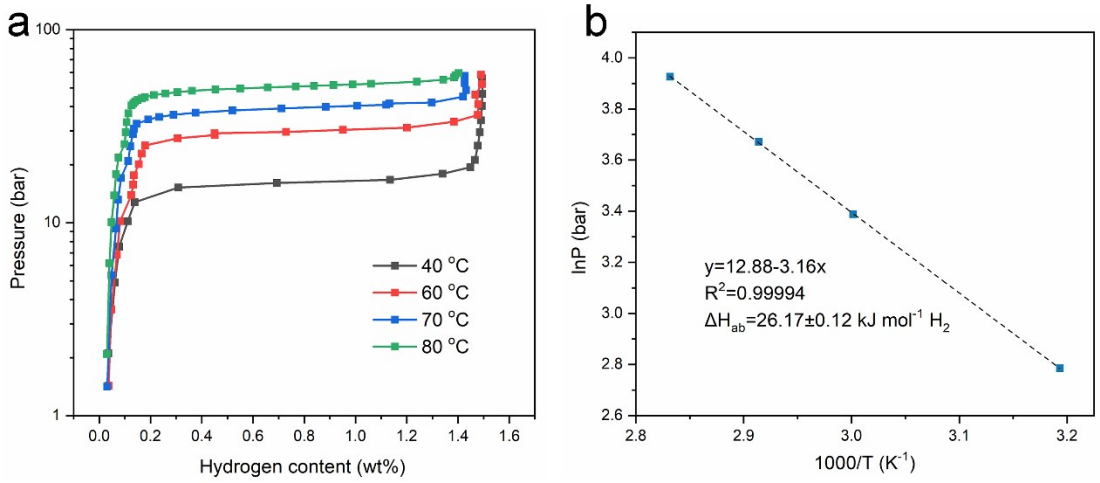

Fig. S1 (a) PCI curves of TiCrMnFeZr composite (after 20 cycles) obtained at 40, 60, 70 and 80 °C, and corresponding (b) van't Hoff fitting plot.

Fig. S2 Photos of as-received (left) and activated (right) 3 g TiCrMnFeZr HEA sample.

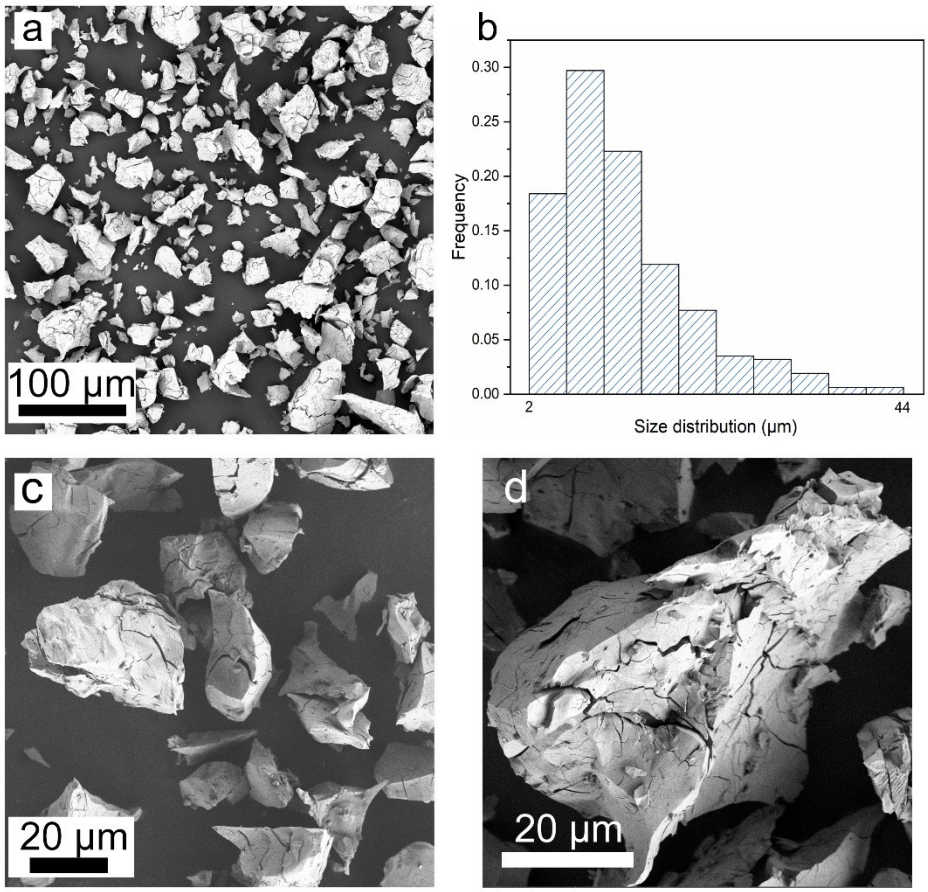

Fig. S3 Typical SEM images of activated TiCrMnFeZr HEA and its particle size distribution.

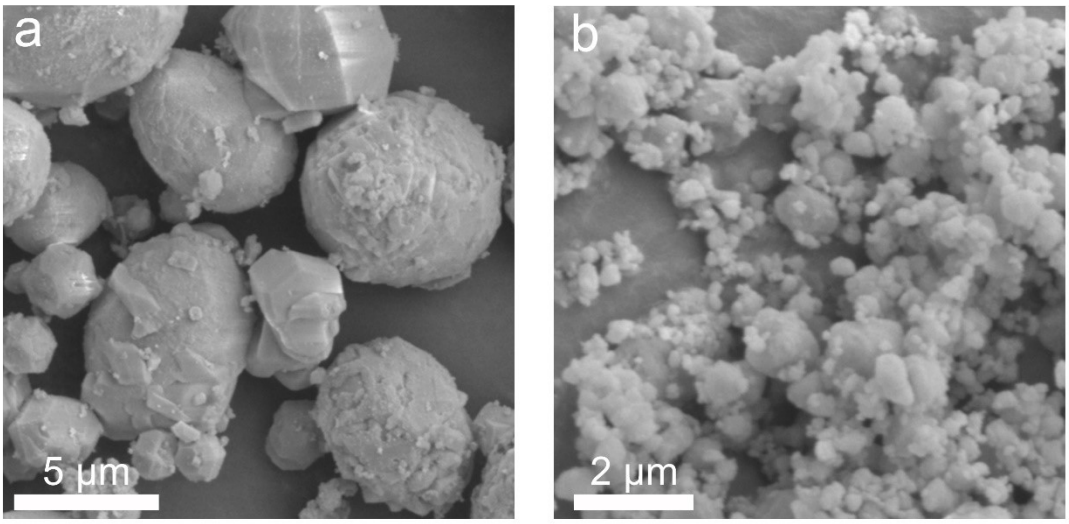

Fig. S4 Typical SEM images of (a) as-received and (b) pure BM MgH_2.

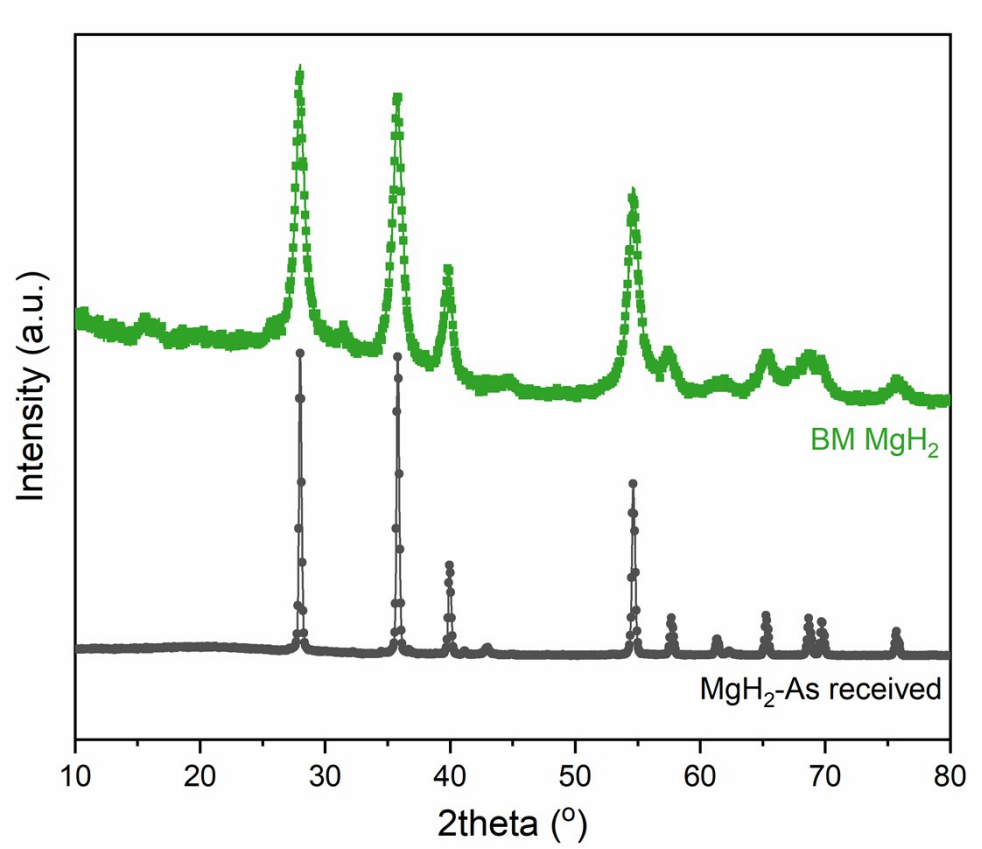

Fig. S5 XRD patterns of as-received and BM MgH_2.

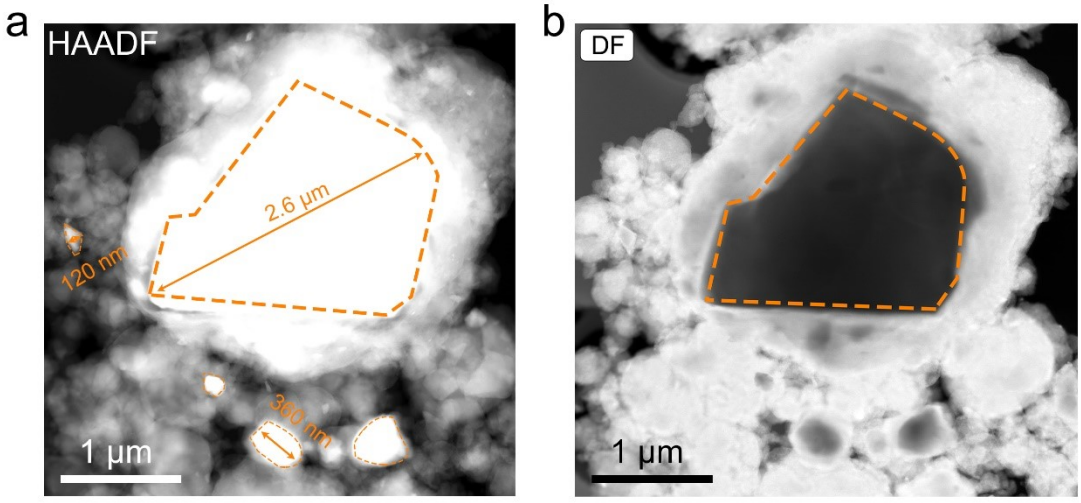

Fig. S6 (a) HAADF and DF images of MgH_2-40 wt% TiCrMnFeZr composites with micrometer TiCrMnFeZr particles.

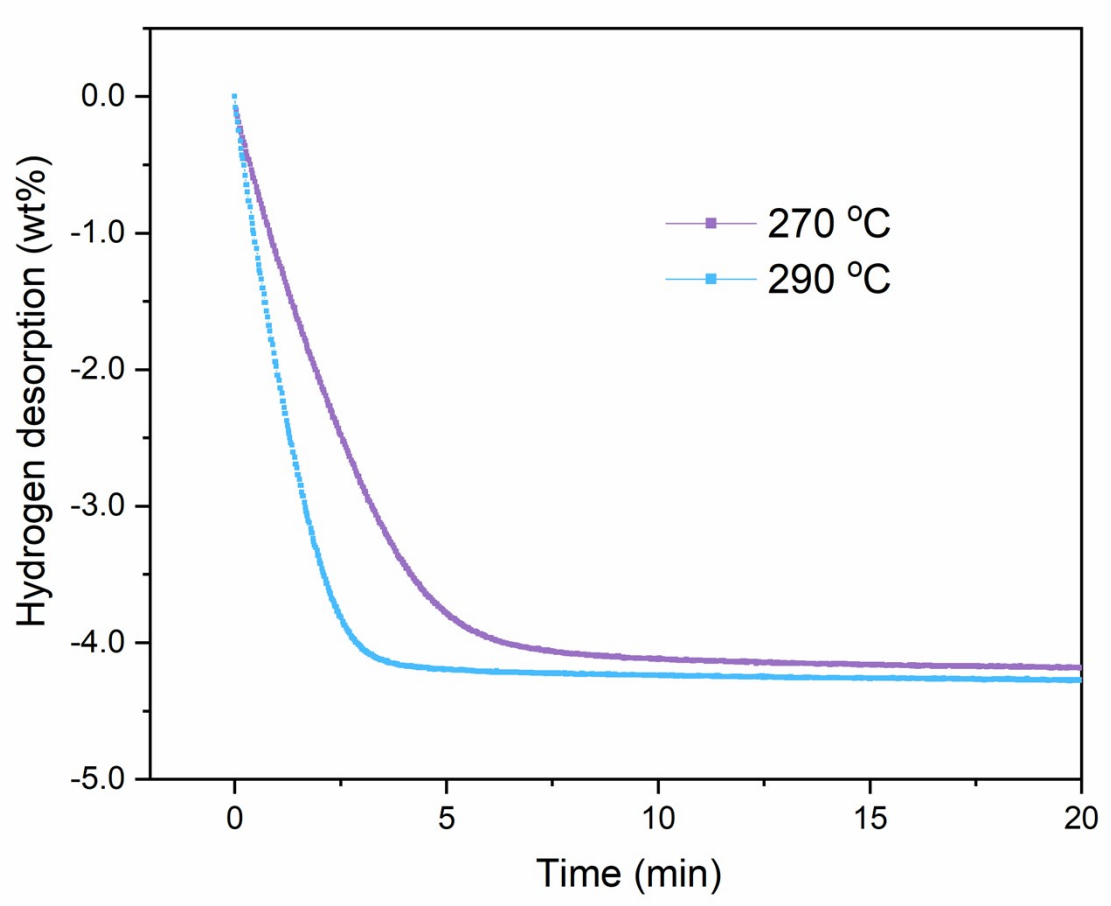

Fig. S7 Isothermal desorption curves of the MgH_2-40 wt% TiCrMnFeZr composite at 270 and 290 °C.

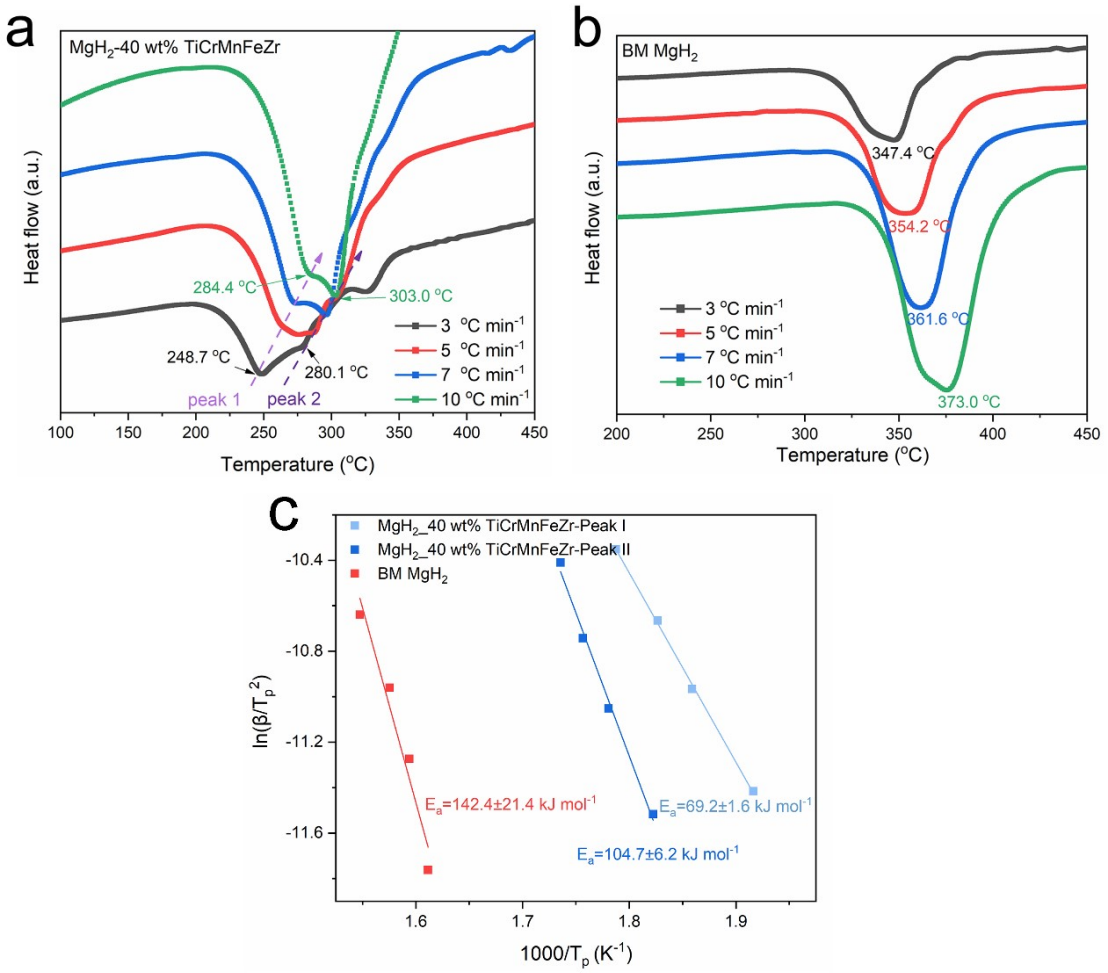

Fig. S8 DCS curves of (a) MgH_2-40 wt% TiCrMnFeZr composite and (b) BM MgH_2, and the (c) corresponding Kissinger's plots.

Table S2 Kinetic mechanism model of composites according to different kinetic models [1, 2]

	Model	Integral form $g(\alpha) = kt$	Sharp's expression
Diffusion models	1D diffusion (D1)	α^2	$0.2500(t/t_{0.5})$
	2D diffusion (D2)	$((1-\alpha)\ln(1-\alpha)) + \alpha$	$0.1534(t/t_{0.5})$
	3D diffusion (Jander equation) (D3)	$(1-(1-\alpha)^{1/3})^2$	$0.0426(t/t_{0.5})$
	3D diffusion (Ginstling-Brounshtein equation) (D4)	$1-(2/3)\alpha-(1-\alpha)^{2/3}$	$0.0367(t/t_{0.5})$
Reaction-order models	First-order (F1)	$-\ln(1-\alpha)$	$-0.6931(t/t_{0.5})$
Geometrical contraction models	Contracting area (R2)	$1-(1-\alpha)^{1/2}$	$0.2929(t/t_{0.5})$
	Contracting volume (R3)	$1-(1-\alpha)^{1/3}$	$0.2063(t/t_{0.5})$
Nucleation models	Avrami−Erofeyev (A2)	$[-\ln(1-\alpha)]^{1/2}$	$0.8326(t/t_{0.5})$
	Avrami−Erofeyev (A3)	$[-\ln(1-\alpha)]^{1/3}$	$0.8850(t/t_{0.5})$

The activation energies are related with the kinetic models used for fitting. To obtain more accurate activation energy values, an in-depth analysis of de/re-hydrogenation kinetic mechanism model of composites was carried out according to nine different kinetic models proposed by Sharp and Jones [1], and the activation energy was fitted according to a suitable kinetic model. The specific methods are provided bellow:

$$d\alpha/dt=k(T)g(\alpha)$$

$$g(\alpha)=A(t/t_{0.5})$$

where α, T, k(T), g(α), A, and $t_{0.5}$ represent the reaction fraction, the reaction temperature, the reaction rate constant, the function depending on the specific kinetic mechanism, the constant related to the kinetic mechanism, and the time when α=0.5, respectively. Through plotting the de/re-hydrogenation experimental data of $t/t_{0.5}$ against the theoretical ones for nine different kinetic models, respectively, the corresponding reliable kinetic model can be obtained (the line with a slope close to 1 is the reliable kinetic model). The integral forms g(α)=kt and Sharp's expressions are given in Table S2, as well as the corresponding desorption models.

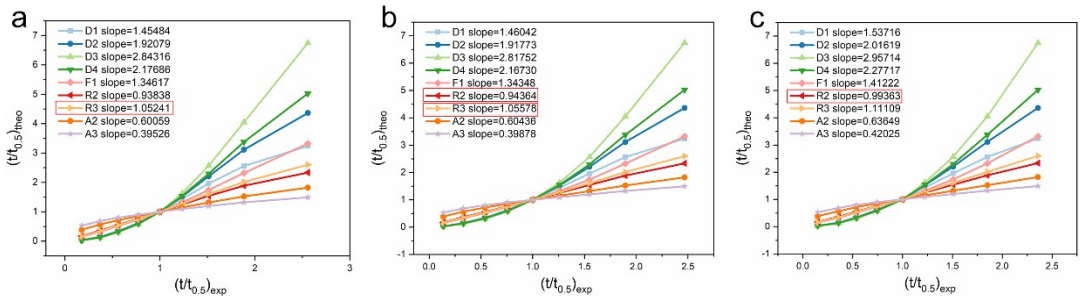

Fig. S9 $(t/t_{0.5})_{theo}$ vs. $(t/t_{0.5})_{exp}$ of the MgH_2-40 wt% TiCrMnFeZr composite at (a) 250, (b) 270, (c) 290 ^oC using various kinetic models.

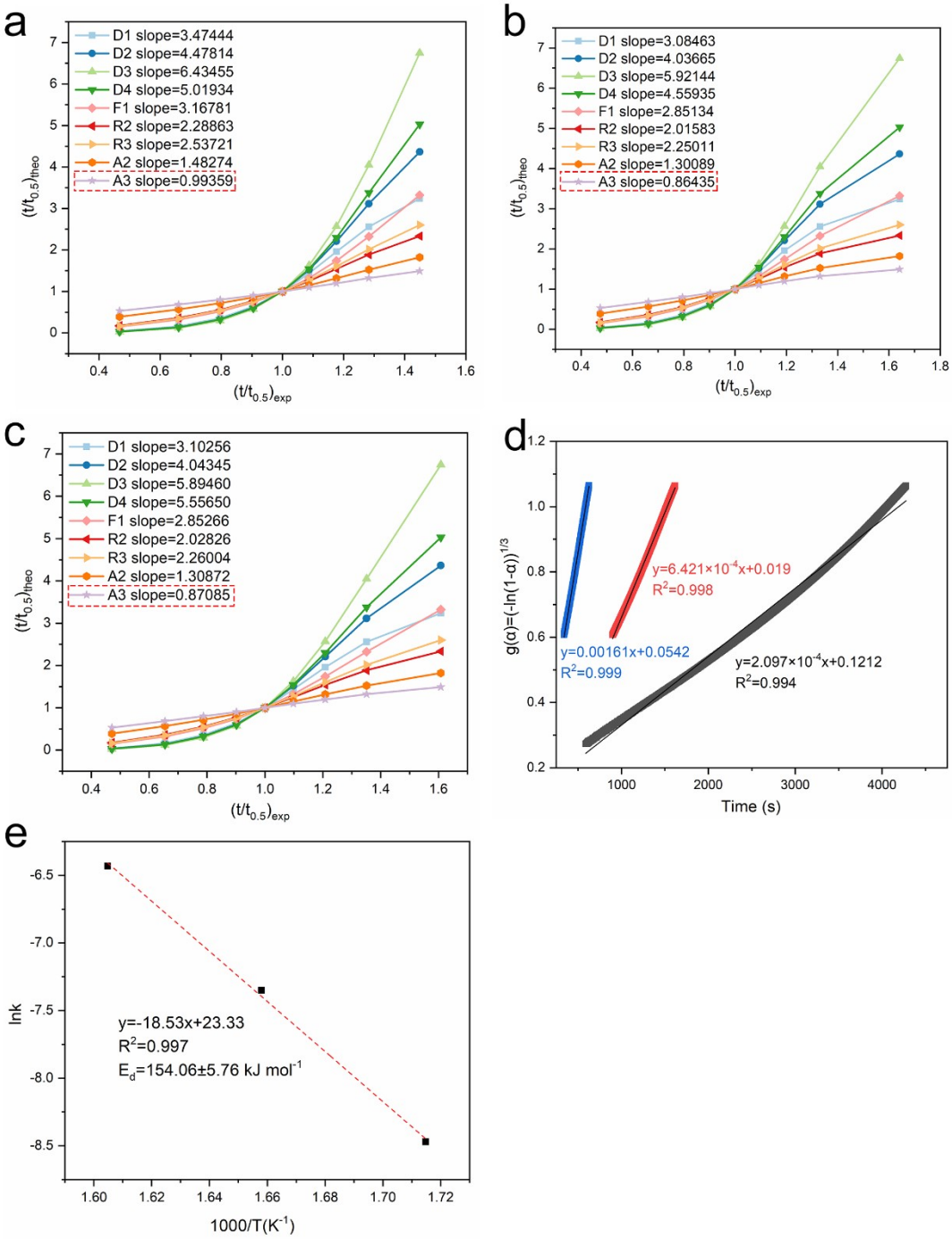

Fig. S10 (a-c) $(t/t_{0.5})_{theo}$ vs. $(t/t_{0.5})_{exp}$ of the BM MgH_2 at 310, 330, 350 °C using various kinetic models. (d) Time dependence of kinetic modeling equation $g(\alpha)= (-\ln (1-\alpha))^{1/3}$ for BM MgH_2 with $0.2 < \alpha < 0.7$ at different temperatures, and (e) Arrhenius plot for the dehydriding kinetics of BM MgH_2.

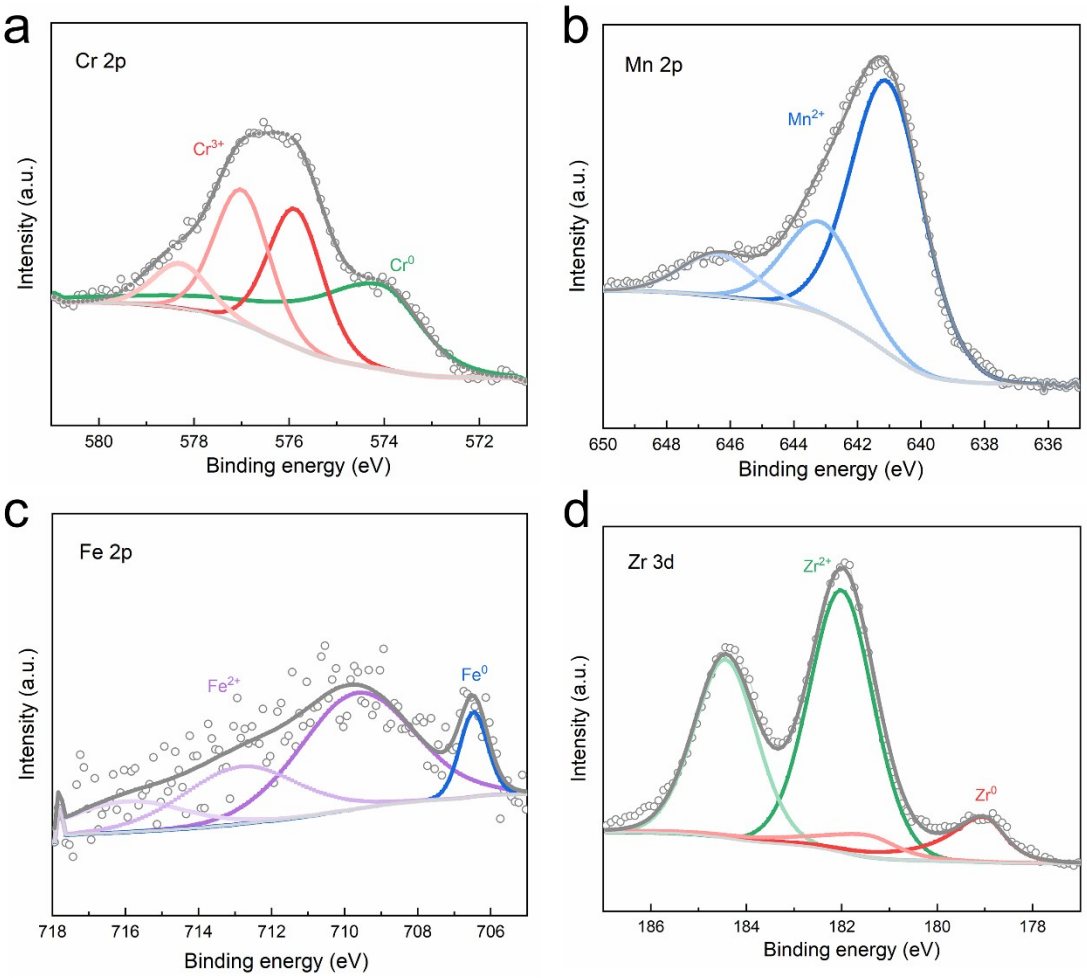

Fig. S11 High-resolution (a) Cr 2p, (b) Mn 2p, (c) Fe 2p, (d) Zr 3d XPS spectra of activated TiCrMnFeZr TEA.

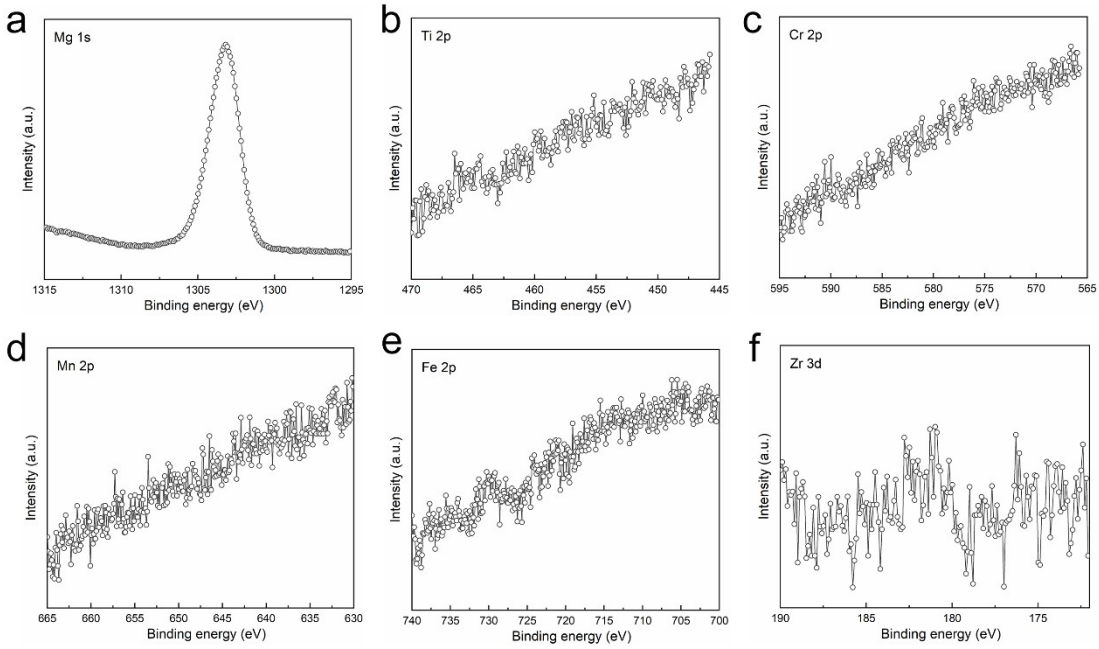

Fig. S12 High-resolution (a) Mg 1s, (b) Ti 2p, (c) Cr 2p, (d) Mn 2p, (e) Fe 2p, (f) Zr 3d XPS spectra of as-synthesis MgH_2- 40 wt% TiCrMnFeZr TEA composite.

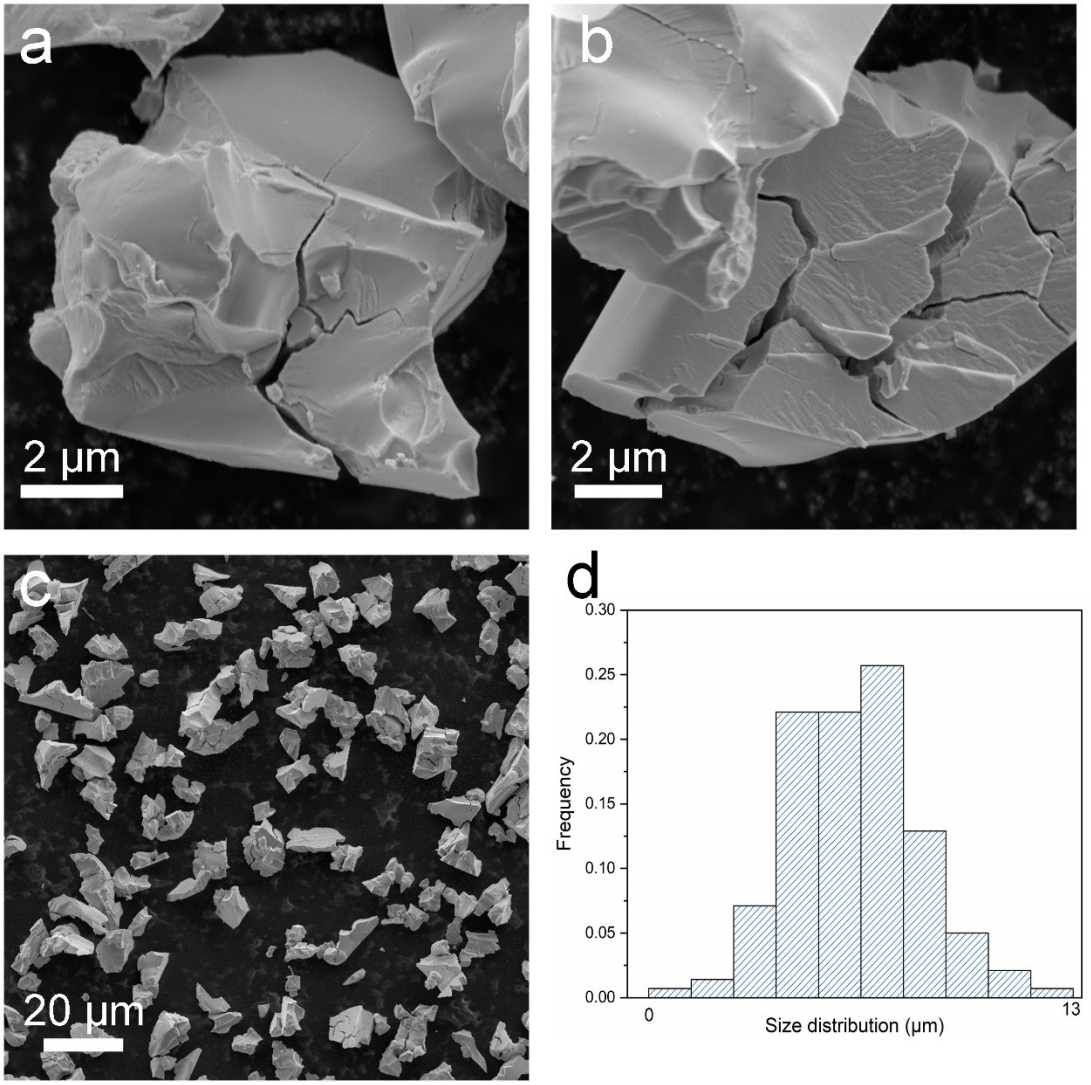

Fig. S13 Typical SEM images of TiCrMnFeZr HEA after 20 cycles and its particle size distribution.

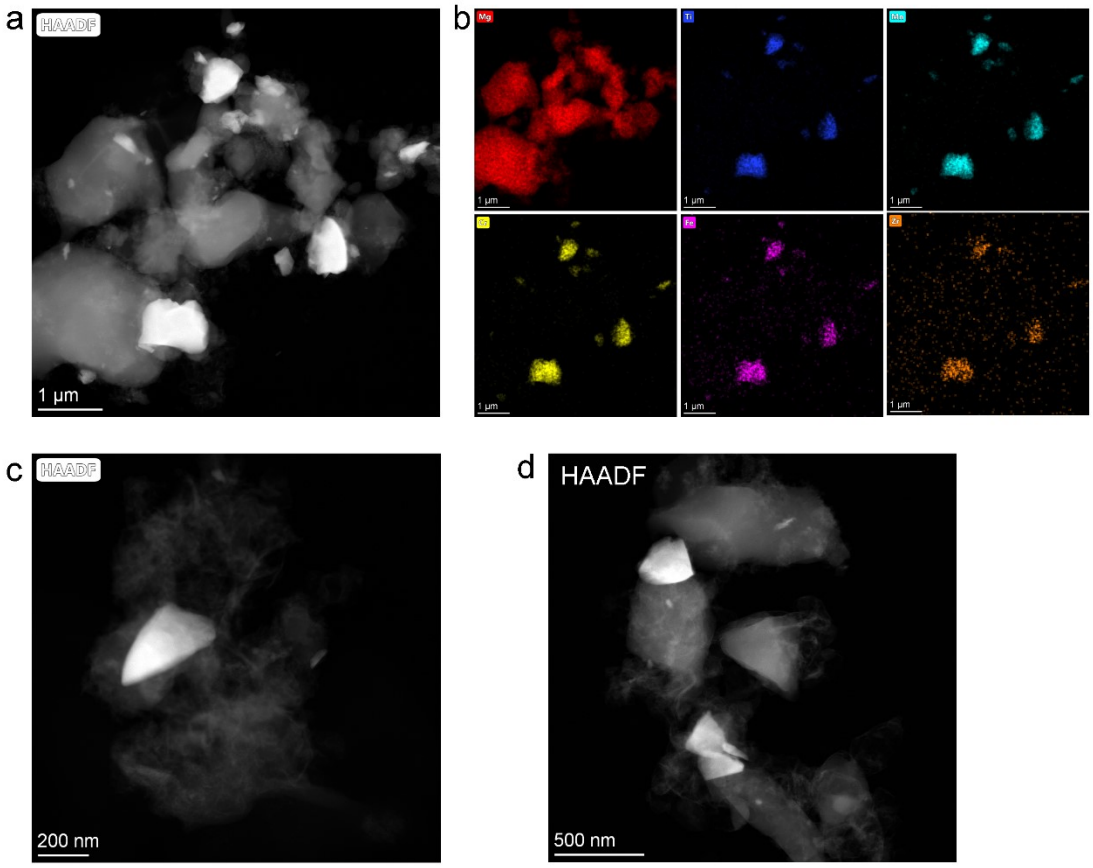

Fig. S14 (a) HAADF images and corresponding (d) STEM elements mapping, (c, d) HAADF images in different parts.

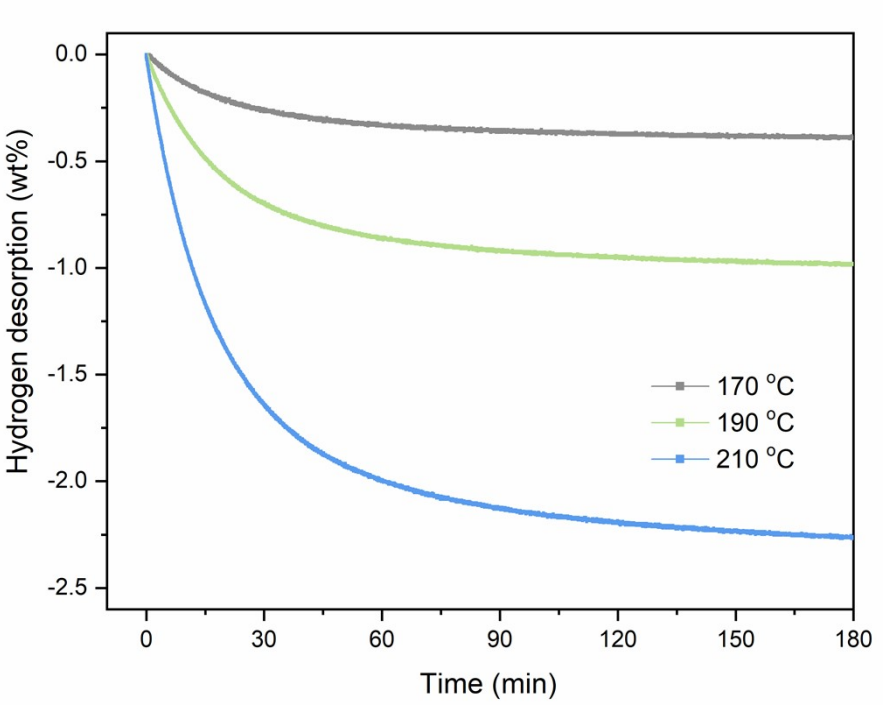

Fig. S15 Isothermal desorption curves of the MgH_2-40 wt% TiCrMnFeZr composite at 170, 190 and 210 °C within 180 min.

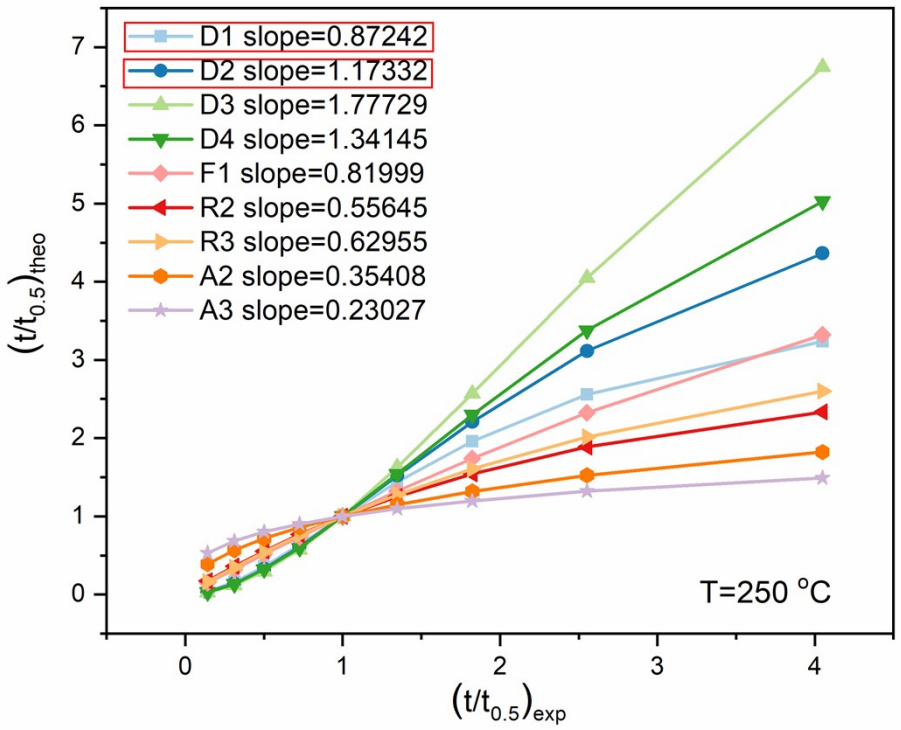

Fig. S16 $(t/t_{0.5})_{theo}$ vs. $(t/t_{0.5})_{exp}$ of the BM MgH_2 at 250 °C for absorption based on various kinetic models.

Table S3. Hydrogen sorption performances comparison of different MgH_2-alloys hydrogen storage composites.

Catalysts and doping amount	Onset desorption temperature	Initial desorption rate	Kinetic desorption performances	Cyclic performance	Ball-milling parameters	reference
TiCrMnFeZr, 40 wt%	162 °C	0.31 wt %/min at 230 °C	290 °C /3 min, 4.0 wt%	100% remaining after 20 cycles	250 rpm/6h, planetary	This work
$(TiVZrNb)_{83}Cr_{17}$, 6 wt%	202 °C	0.008 wt%/min at 250 °C	300 °C/60 min, 4.1 wt%	97.6% remaining after 10 cycles	400 rpm/12 h, -	3
TiMgVNi, 5wt%	-	0.18 wt%/min at 275 °C	300 °C/200 min, 6.2 wt%	92% remaining after 50 cycles	400 rpm/100h, planetary	4
TiFe, 10wt%	180 °C	0.21 wt %/min at 250 °C	300 °C/10 min, 6.6 wt%	87.9% remaining after 10 cycles	450 rpm/5h, planetary	5
ZrTiNiFeVMn, 10wt%	240 °C	0.2 wt%/min at 275 °C	300 °C/20 min, 6.5 wt%	92% remaining after 30 cycles	400 rpm/20h, -	6
FeCoNiLa, 10wt%	-	0.2 wt%/min, 275 °C	300 °C/20 min, 6.23 wt%	98.2% remaining after 20 cycles	450 rpm/6h, -	7
FeCoNiCrTi, 10wt%	199 °C	0.13 wt %/min at 230 °C	290 °C /10 min, 6.6 wt%	94.2% remaining after 20 cycles	400 rpm/4h, planetary	8
TiVNbCr, 5wt%	-	0.06 wt%/min at 250 °C	300 °C/20 min, 6 wt%	-	30h, vibratory	9
NiCoFeCuMg, 10 wt%	-	0.5 wt%/min at 275 °C	300 °C/30 min, 6.12 wt%	97% remaining after 20 cycles	400 rpm/4h, -	10
TiVNbZrFe, 10 wt%	210 °C	0.857 wt%/min at 270 °C	300 °C/5 min, 5.7 wt%	94.6% remaining after 15 cycles, then gradually increasing	-/4h, planetary	11
FeCoNiCrMn, 5 wt%	209 °C	0.813 wt%/min at 280 °C	300 °C/4 min, 5.8 wt%	98.6% remaining after 50 cycles	280 rpm/10h, planetary	12
TiZrMnCrV, 10 wt%	237 °C	0.33 wt%/min at 300 °C	300 °C/20 min, 2.5 wt%	95.3% remaining after 50 cycles	400 rpm/5h, -	13
CrMnFeCoNi, 10 wt%	198 °C	0.875 wt%/min at 270 °C	300 °C/8 min, 6.0 wt%	96.6% remaining after 10 cycles	400 rpm/6h, -	14
AlCrMnFeCoNi, 7wt%	338 °C	1.1 wt%/min at 300 °C	300 °C/60 min, 6.2 wt%	99.5% remaining after 25 cycles	200 rpm/24h, planetary	15
Nano $ZrMn_2$, 10wt%	182 °C	1.5 wt %/min at 300 °C	300 °C/5 min, 6.8 wt%	-	450 rpm/5 h, -	16

Reference

1. J. Sharp, G.W. Brindley and B.N. Narahari Achar, *Journal of the American Ceramic Society*, 1966, **49**, 379-382.
2. A. Khawam, D. R. Flanagan, Solid-State Kinetic Models: Basics and Mathematical Fundamentals, *The Journal of Physical Chemistry B*, 2006, **110**,17315-17328.
3. M. Wei, Y. Liu, X. Xing, Z. Zhang and T. Liu, *Chemical Engineering Journal*, 2023, **476**, 146639.
4. C. Hu, Z. Zheng, T. Si and Q. Zhang, *International Journal of Hydrogen Energy*, 2022, **47**, 3918-3926.
5. X. Lu, L. Zhang, H. Yu, Z. Lu, J. He, J. Zheng, F. Wu and L. Chen, *Chemical Engineering Journal*, 2021, **422**, 130101.
6. F. Yin, Z. Chen, T. Si, D. Liu, Y. Li, H.-W. Li and Q. Zhang, *Journal of Alloys and Compounds*, 2024, **997**, 174822.
7. Y. Jiang, Y. Liu, M. Yue, Y. Sun, Y. Cao, Q. Yuan and Y. Wang, *Journal of Energy Storage*, 2025, **107**, 114956.
8. M.-C. Song, F.-Y. Wu, Y.-Q. Jiang, X.-Z. Wang, H. Zhao, L.-X. Chen and L.-T. Zhang, *Rare Metals*, 2024, **43**, 3273-3285.
9. T. Si, F. Yin, X. Zhang, Q. a. Zhang, D. Liu and Y. Li, *Scripta Materialia*, 2023, **222**, 115052.
10. Y. Liu, M. Yue, Y. Guo, Y. Jiang, Y. Sun, L. Feng and Y. Wang, *Journal of Magnesium and Alloys*, 2025, **13**, 1232-1242.
11. J. Zhang, H. Liu, C. Zhou, P. Sun, X. Guo and Z. Z. Fang, *Journal of Materials Chemistry A*, 2023, **11**, 4789-4800.
12. H. Wan, X. Yang, S. Zhou, L. Ran, Y. Lu, Y. a. Chen, J. Wang and F. Pan, *Journal of Materials Science & Technology*, 2023, **149**, 88-98.
13. Z. Zhang, Y. Cheng, Z. Yu, W. Wang, Y. Li, Z. Liu and S. Han, *ACS Sustainable Chemistry & Engineering*, 2024, **12**, 17702-17712.
14. L. Wang, L. Zhang, X. Lu, F. Wu, X. Sun, H. Zhao and Q. Li, *Chemical Engineering Journal*, 2023, **465**, 142766.
15. S. K. Verma, S. S. Mishra, N. K. Mukhopadhyay and T. P. Yadav, *International Journal of Hydrogen Energy*, 2024, **50**, 749-762.
16. L. Zhang, Z. Cai, Z. Yao, L. Ji, Z. Sun, N. Yan, B. Zhang, B. Xiao, J. Du, X. Zhu and L. Chen, *Journal of Materials Chemistry A*, 2019, **7**, 5626-5634.